

**Single Cu–N<sub>4</sub> sites enable atomic Fe clusters with high-performance oxygen reduction reaction**

Shuwen Wu,<sup>a</sup> Shang Jiang,<sup>a</sup> Shao-Qing Liu,<sup>a</sup> Xuehai Tan,<sup>a</sup> Ning Chen, Jing-Li Luo,<sup>a</sup> Samir H. Mushrif,<sup>a</sup> Ken Cadien<sup>a</sup> and Zhi Li<sup>a\*</sup>

- a. Department of Chemical and Materials Engineering,  
University of Alberta, Edmonton, AB T6G 2V4, Canada  
E-mail: zhi.li@ualberta.ca
  
- b. Hard X-Ray MicroAnalysis BL, Canadian Light Source, 44 Innovation Boulevard  
Saskatoon, SK S7N 2V3, Canada

## Experimental section

**Synthesis of Cu/ZIFs-8.** 1.041 g  $\text{Zn}(\text{NO}_3)_2 \cdot 6\text{H}_2\text{O}$  and 0.0954 g  $\text{Cu}(\text{NO}_3)_2 \cdot 3\text{H}_2\text{O}$  were dissolved in 8 mL deionized (DI) water. 22.7 g 2-methylimidazole was dissolved in 80 mL DI water. Then these two aqueous solutions were purified by filter paper before mixing. The purified nitrate solution was subsequently poured into the above 80 mL of the solution containing 22.7 g 2-methylimidazole with magnetically stirring for 5 min at room temperature. The products were collected by centrifugation (12000 rpm, 30 min) and washed by DI water at least three times. The product was dried at 60 °C overnight in a vacuum drying oven.

**Synthesis of  $\text{Fe}_x/\text{Cu-N@CF}$ ,  $\text{Cu-N@CF}$  and  $\text{Fe}_x\text{-N@CF}$ .** The main membrane was synthesized via an electrospinning process. First, 330 mg of polyacrylonitrile (PAN,  $M_w = 150,000$ ), 770 mg of Cu/ZIFs-8 and 200 mg of melamine were dissolved in 8 mL of N, N-dimethylformamide (DMF) in a round bottom flask via vigorously stirring at 60 °C overnight to get a homogenous precursor mixture. The precursor solution was diverted into a syringe with a stainless tip needle for the subsequent electrospun process. The processing condition was 0.7 mL/h of solution flow rate, 21 kV of applied potential and 15 cm of spin distance. The as-spun fibers were peroxidized in the air at 250 °C for 1 h, following carbonized under Ar gas at a high temperature of 900 °C for 2 h with 5 °C  $\text{min}^{-1}$  heating rate. After this carbonization, the atomically dispersed Cu anchored N-doped porous carbon fibers ( $\text{Cu-N@CF}$ ) was formed. Then, the deposition of Fe atoms was conducted on the above resultant material. In a typical process, 40 mg of anhydrous  $\text{FeCl}_3$  was placed in a boat sitting in the tube upstream of the gas flow; 40 mg of the carbonized material was placed in another boat sitting in the tube downstream of the gas flow. The furnace was heated to 750 °C with a ramping rate of 10 °C  $\text{min}^{-1}$  and maintained at this temperature for 3 h under the continuous Ar gas flow (100 mL  $\text{min}^{-1}$  of flow rate). Then the  $\text{Fe}_x/\text{Cu-N@CF}$  was collected.  $\text{Fe}_x\text{-N@CF}$  was prepared in a similar way by using pristine ZIF-8 for electrospinning.

**Materials characterization.** The morphologies of prepared materials were studied via Zeiss Sigma 300 VP-Field Emission Scanning Electron Microscopy (FESEM) and Transmission electron microscopy (TEM) on a JEOL JEMARM200CF equipped with an energy dispersive spectrometer (EDS). Atomic-resolution electron energy-loss spectroscopy (EELS) images were taken with a Titan Cubed Themis G20 TEM equipped with a highly sensitive Super-X energy dispersive X-ray detector system (operated at 300 kV). The crystal structure was characterized by X-ray diffractometer (XRD, D8 discover diffraction system equipped with

Cu K $\alpha$  radiation (40 kV, 44 mA)) at a scan rate of 5° min<sup>-1</sup>. Nitrogen adsorption-desorption isotherms were collected on an Autosorb Quantachrome 1MP at 77 K. X-ray photoelectron spectroscopy (XPS) spectra were performed on Kratos Analytical AXIS 165 with a monochromatic Al K $\alpha$  source to study the chemical compositions. The C 1 s photoelectron peak at 284.6 eV as reference was used for spectrometer calibration. The Fe/Cu ratio was determined by inductively coupled plasma optical emission spectrometry (ICP-OES) on Thermo iCAP6300 Duo ICP\_OES.

**XAFS measurements and data analysis.** The local structures of the investigated materials were analyzed by measuring the Fe K-edge and Cu K-edge X-ray absorption near-edge structure (XANES) and the extended X-ray absorption fine structure (EXAFS) data at the Hard X-ray microanalysis beamline (HXMA-061D) of the Canadian Light Source. The X-ray absorption spectra were acquired in fluorescence mode using a Si(111) double-crystal monochromator to range the X-ray energy from 5–40 keV. The ring current is 250 mA. A He-filled Oxford straight ion chamber detector was used to monitor the incident X-ray, and the fluorescence yield signal was captured using a 32-element Ge detector. The energy was calibrated using Fe and Cu plate reference samples. The obtained XAFS raw data were normalized, background-subtracted, and Fourier transformed based on the standard procedures using the ATHENA program.<sup>1, 2</sup> The k<sup>2</sup>-weighted EXAFS spectra were obtained by normalizing to the edge-jump step and subtracting the post-edge background from the overall absorption. Then,  $\chi(k)$  data of Fe and Cu K edge in the k-space was Fourier transformed to real (R) space using a Hanning window ( $dk = 1.0 \text{ \AA}^{-1}$ ) to separate the EXAFS contributions from different coordination shells in k range 3–11  $\text{\AA}^{-1}$ . The EXAFS fitting analysis was performed using the ARTEMIS program according to standard procedures to get the quantitative structural parameters.<sup>2</sup> The WT of EXAFS data was performed by using the Hama Fortran code. The parameters were R range: 1–3  $\text{\AA}$ , k range: 0–15  $\text{\AA}^{-1}$ . Morlet function with  $\kappa = 10$ ,  $\sigma = 1$  was used as the mother wavelet to provide the overall distribution.<sup>3, 4</sup> The theoretical calculation for XANES data was performed with the FDMNES code under the Molecule model with “Quadrupole” and “SCF” included in the calculation.<sup>5, 6</sup>

**Electrochemical measurements of ORR.** Electrochemical measurements were conducted by BioLogic SP-300 electrochemical test station. A Pine instrument (PINE Research MSR Rotator, model: AFMSRCE, USA) was used for ORR measurements by a standard three-electrode system in an O<sub>2</sub>-saturated 0.1 M KOH or 0.1 M HClO<sub>4</sub> electrolyte. A standard three-electrode system comprises working, reference, and counter electrodes in a batch-type electrochemical cell.<sup>7, 8</sup> In our work, a graphite rod and a saturated calomel electrode (SCE)

were employed as the counter electrode and the reference electrode, respectively. For the preparation of the working electrode, 5 mg of catalyst was dispersed in the mixture of 495  $\mu\text{L}$  isopropyl alcohol (IPA), 495  $\mu\text{L}$  DI water and 10  $\mu\text{L}$  Nafion (5 wt%) under sonication to form a homogeneous catalyst ink. Then 10  $\mu\text{L}$  of this catalyst ink was dipped on a glassy carbon disk of RDE with a diameter of 0.5 cm, followed by drying at room temperature. The total weight loading of catalysts for both as-prepared catalysts and commercial Pt/C (20 wt%, Sigma Aldrich) was 0.255  $\text{mg cm}^{-2}$ . The ORR test at an RDE was conducted in  $\text{O}_2$ -saturated 0.1 M KOH electrolytes with varying rotating speeds from 400 to 2025 rpm at a scan rate of 5  $\text{mV s}^{-1}$ . The onset potential was defined as a potential value corresponding to 5 % of the diffusion-limited current density. 10000 potential cycles were conducted to examine the electrocatalytic durability at the sweep speed of 50  $\text{mV s}^{-1}$ . The ORR potentials were calculated into the reversible hydrogen electrode (RHE) by the following equation:

$$E (\text{vs. RHE}) = E (\text{vs. SCE}) + 0.059 \times \text{pH} + 0.241 \quad (1)$$

The electron transfer number ( $n$ ) per oxygen molecule for oxygen reduction can be determined by the Koutechy–Levich equations (2-3):

$$\frac{1}{J} = \frac{1}{J_L} + \frac{1}{J_K} = \frac{1}{B\omega^{0.5}} + \frac{1}{J_K} \quad (2)$$

$$B = 0.62nFC_0(D_0)^{3/2}\nu^{-1/6} \quad (3)$$

where  $J$  is the measured current density,  $J_L$  and  $J_K$  are the diffusion- and kinetic-limiting current densities,  $\omega$  is the electrode rotation rate expressed in angular velocity ( $\text{rad s}^{-1}$ ),  $n$  is the transferred electron number,  $F$  is the Faraday constant ( $96485 \text{ C mol}^{-1}$ ),  $C_0$  is the concentration of  $\text{O}_2$  in the electrolyte ( $1.26 \times 10^{-6} \text{ mol cm}^{-3}$ ),  $D_0$  is the diffusion coefficient of  $\text{O}_2$  ( $1.93 \times 10^{-5} \text{ cm}^2 \text{ s}^{-1}$ ), and  $\nu$  is the kinetic viscosity of 0.1M KOH ( $0.01 \text{ cm}^2 \text{ s}^{-1}$ ).<sup>9</sup>

RRDE measurements were carried out to investigate the electron selectivity of the as-prepared samples with the same catalyst loading as RDE measurement. The model of the RRDE setup is AFE6R1PT with disk OD = 5.0 mm, ring OD = 7.50 mm, ring ID = 6.50 mm. The disk electrode was scanned cathodically under the same condition of RDE at a scan rate of 5  $\text{mV s}^{-1}$  and the ring potential was kept at 1.5 V vs RHE. The rotation rate is 1600 rpm. The following equations (4-5) were used to calculate hydrogen peroxide ( $\text{H}_2\text{O}_2$ ) yield and electron transfer number ( $n$ ).

$$n = \frac{4I_D}{I_D + I_R/N} \quad (4)$$

$$\text{H}_2\text{O}_2\% = \frac{2I_R/N}{I_D + I_R/N} \times 100 \quad (5)$$

where  $I_D$  is disk current,  $I_R$  is ring current, and  $N \approx 0.25$  is the current collection efficiency of the Pt ring, which was provided by the manufacturer.

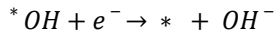
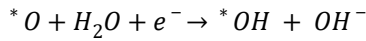
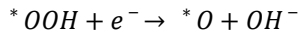
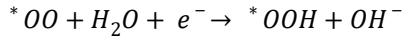
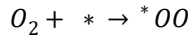
**Zn–air battery (ZAB) performance test.** The ZAB tests were carried out using a homemade electrochemical cell. The ability of the electrocatalysts to serve as an air electrode in ZAB was evaluated under ambient conditions. A polished zinc foil was used as the anode. 5 mg of the prepared catalyst was dispersed in 1 mL DI water, 3 mL IPA and 1 mL Nafion via probe sonication. The cathode was prepared by drop casting the catalyst inks onto the Gas Diffusion Layer (GDL) of carbon fiber paper with a mass loading of  $0.5 \text{ mg cm}^{-2}$ . For the primary Zn-air batteries, the electrolyte consists of 6 M KOH and 0.2 M zinc acetate dehydrate.  $\text{Fe}_x/\text{Cu-N@CF+IrO}_2$  (w:w = 1:1) ink was prepared in the same way for the long-term charge-discharge cycle stability test of the ZAB device in that it was performed with a period of 10 min charge and 10 min discharge. For all-solid-state Zn–air battery assembly, the gel polymer electrolyte was prepared as follows. Polyvinyl alcohol (PVA, 1 g) was dissolved in 10 mL DI water under continuous stirring at  $95 \text{ }^\circ\text{C}$  to form a homogeneous gel. Then 1 mL of 18 M KOH containing 0.2 M zinc acetate dehydrate was added dropwise to form a homogeneous viscous solution. The as-prepared  $\text{Fe}_x/\text{Cu-N@CF}$  film and zinc foil were placed on the two sides of the PVA gel, followed by pressed Ni foam as the current collector. The reference cathode was made in the similar way using commercial Pt/C or Pt/C+IrO<sub>2</sub> (w:w=1:1).

### Computational methods

DFT calculations were performed with the periodic plane-wave implementation (with the plane-wave cutoff energy of 450 eV) of DFT using the Vienna Ab-initio Simulation Package (VASP)<sup>10-13</sup> with the projector augmented wave (PAW) scheme.<sup>14,15</sup> The Perdew-Burke-Ernzerhof (PBE) exchange correlation functional<sup>16</sup> with the vdW-DFT<sup>17,18</sup> was used as the Generalized gradient approximation (GGA).  $3 \times 3 \times 1$  K-point sampling and within the Monkhorst-Pack scheme was used for integration over the Brillouin zone. The convergence criteria for total energy and inter-atomic forces of all calculations were  $10^{-6}$  eV per unit cell and  $0.01 \text{ eV } \text{Å}^{-1}$ , respectively. A 15 Å vacuum thickness above the top layer was used to prevent the interaction between repeated periodic unit cells. To obtain the free energies of the ORR reaction intermediates, the entropy, zero-point energy and enthalpy correction were computed from statistical thermodynamics for all adsorbed structures, while those values for gas-phase molecules were taken from the standard thermodynamics NIST-JANAF table.<sup>19</sup>

The reaction energy of the entire ORR process is calculated according to the method proposed by Norskov et al.<sup>20</sup>

The four-electron ORR pathway was simulated as follows:



The asterisk \* represents the adsorption site.

For each reaction step, the Gibbs reaction free energy is calculated as

$$\Delta G = \Delta E + \Delta ZPE - T\Delta S - eU + \Delta E_{pH}$$

where  $\Delta E$  is the reaction energy between the reactants and products;  $\Delta ZPE$  is the change in zero-point energy due to the reaction; T is the temperature and  $\Delta S$  is the change in entropy ;  $-eU$  includes the bias effect on all states involving the electron in the electrode, where e is the transferred charge and U is the electrode potential;  $\Delta E_{pH}$  is the energy correction due to pH value of the electrolyte, which depends on the concentration of  $H^+$ :

$$\Delta G_{pH} = -kT \ln[H^+]$$

where k is the Boltzmann constant and T is the temperature. The Gibbs reaction free energy were calculated for each reaction step.

The free energy of gas-phase  $O_2$  molecule was determined as

$$G_{O_2(g)} = 4 \times 1.23eV + 2G_{H_2O} - 2G_{H_2}$$

The zero-point energies were obtained by vibrational frequency calculations and the zero-point energy of the adsorption site was assumed negligible. The thermodynamic properties of

gas-phase molecules were taken from the standard thermodynamics NIST-JANAF table, and the entropies of adsorbates and adsorption site were assumed to be negligible. All reported free energies of gas phase and reaction free energies were computed at 20 °C.

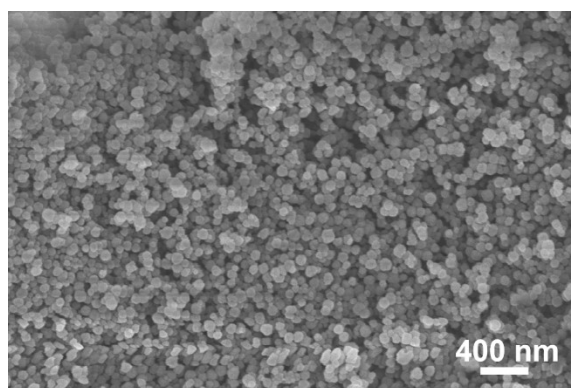


Figure S1. SEM image of Cu/ZIF-8.

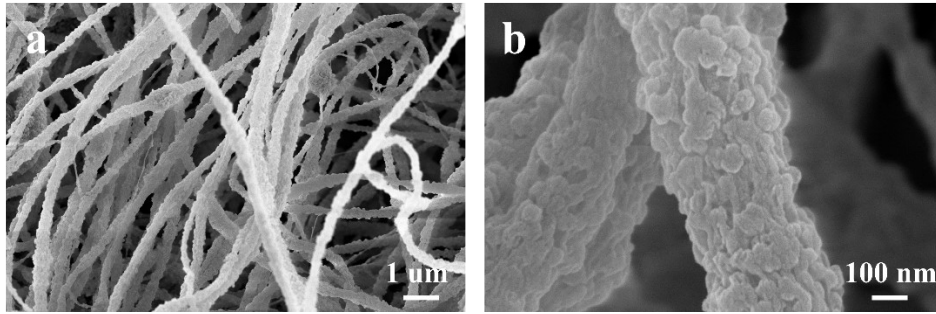


Figure S2. SEM images of Cu/ZIF-8@PF.



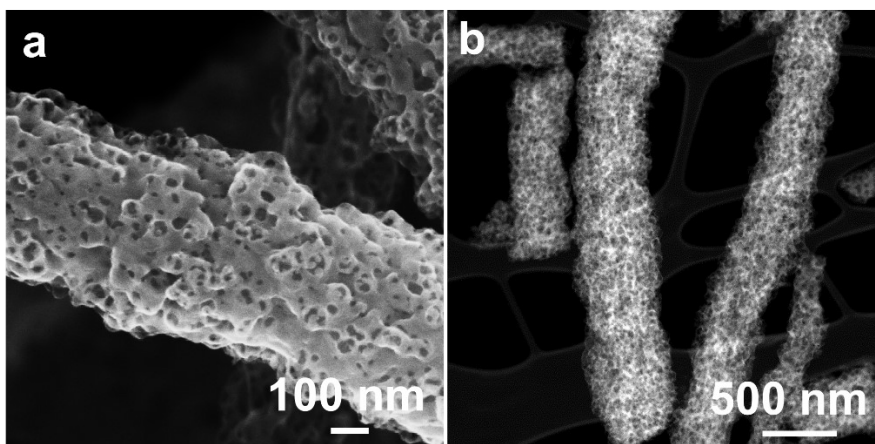


Figure S3. (a) high resolution SEM image, (b) HAADF-STEM image of  $\text{Fe}_x/\text{Cu-N@CF}$ .

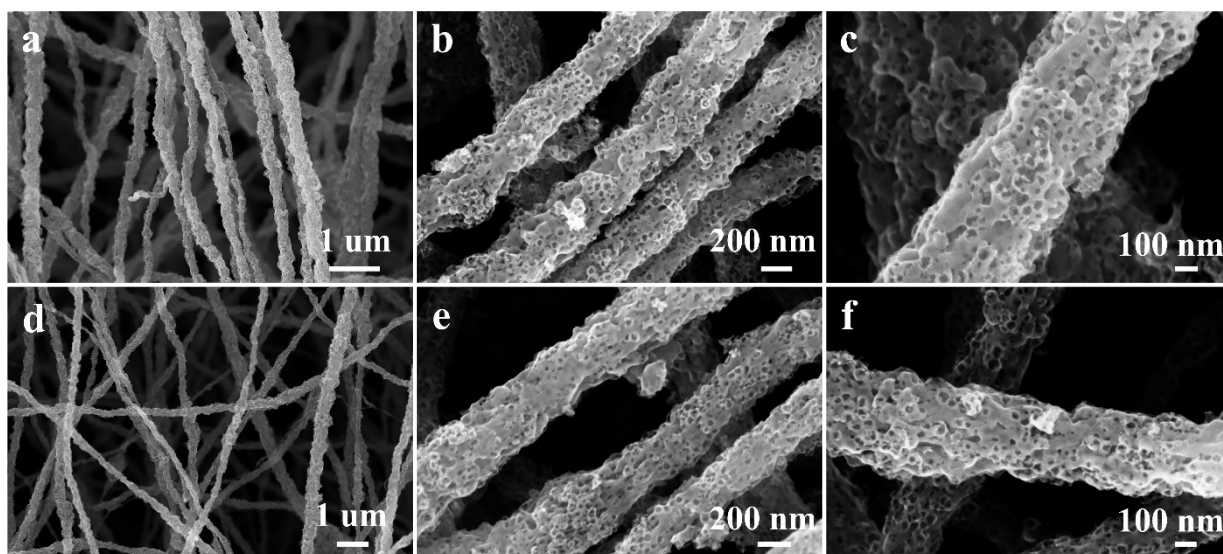


Figure S4. SEM images of (a-c) Cu-N@CF and (d-f) Fe<sub>x</sub>-N@CF.

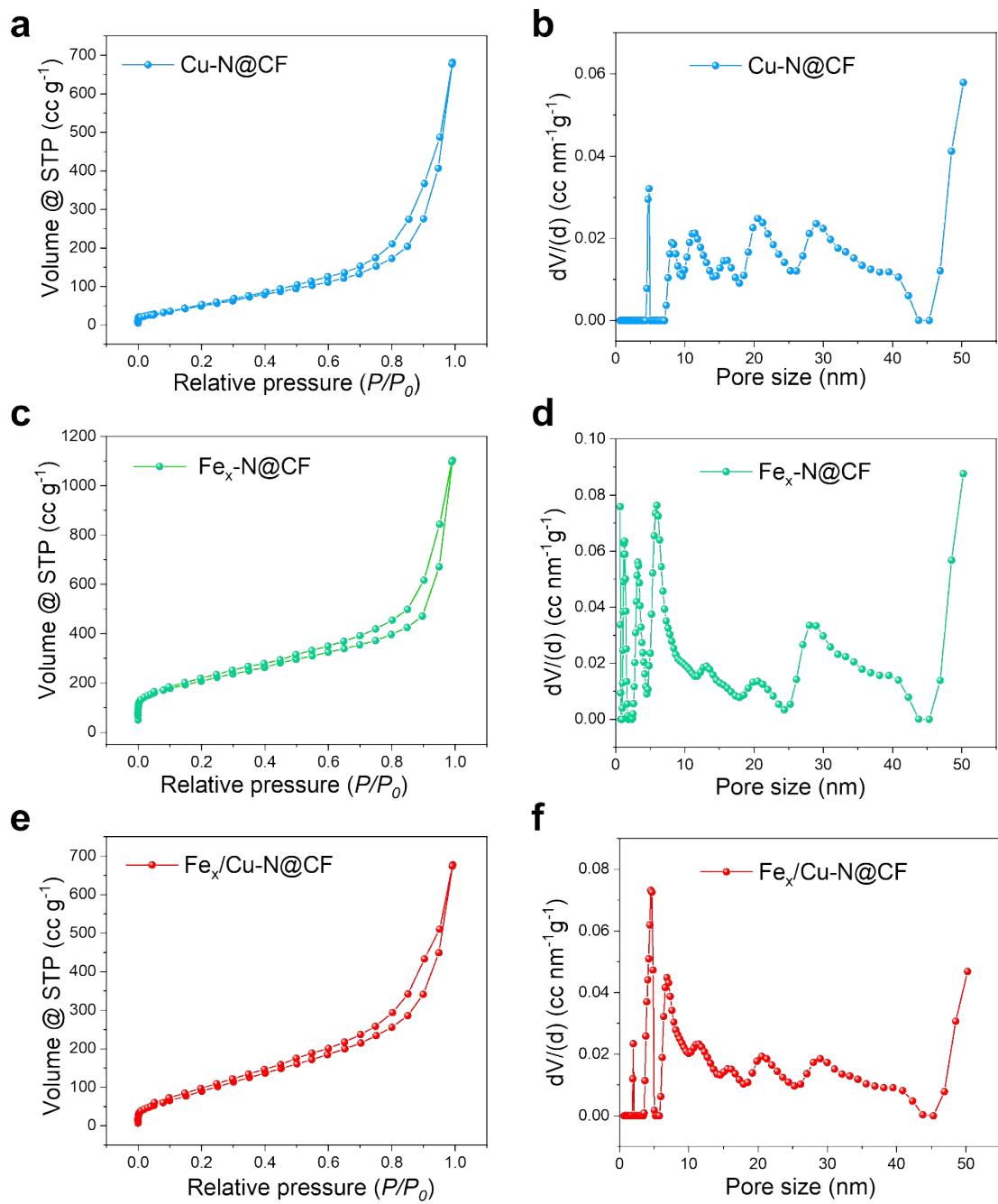


Figure S5. N<sub>2</sub> adsorption isotherms and pore size distributions of (a, b) Cu-N@CF, (c, d) Fe<sub>x</sub>-N@CF and (e, f) Fe<sub>x</sub>/Cu-N@CF.

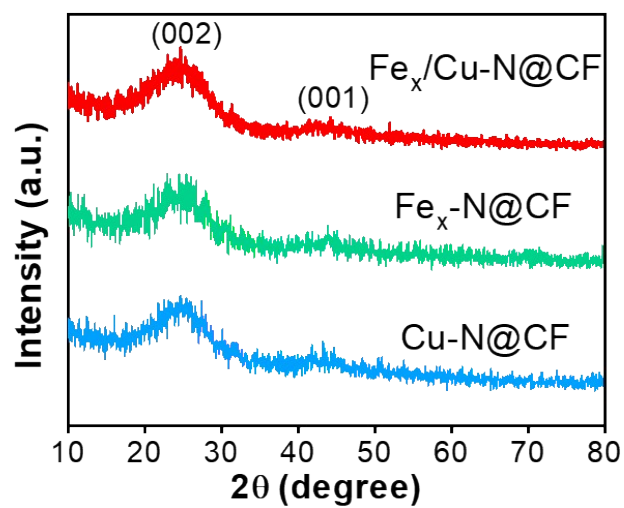


Figure S6. XRD patterns of Cu-N@CF, Fe<sub>x</sub>-N@CF and Fe<sub>x</sub>/Cu-N@CF.

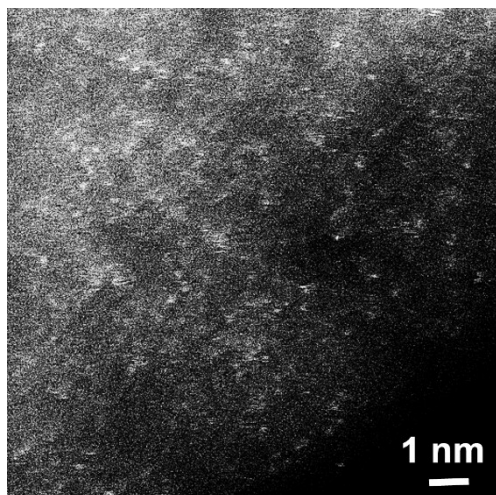


Figure S7. The magnified HAADF-STEM image of Cu-N@C.

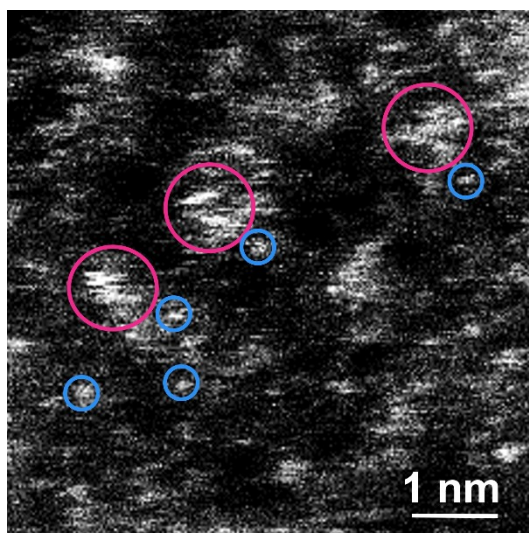


Figure S8. HAADF-STEM image showing the coexistence Fe clusters (marked by pink circles) and single Cu atoms (marked by blue circles) of Fe<sub>x</sub>/Cu-N@CF.

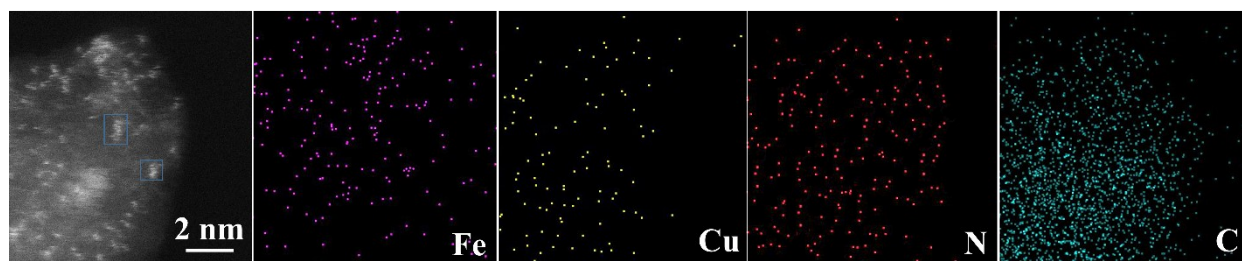


Figure S9. The magnified HAADF-STEM image and corresponding EDS mapping of  $\text{Fe}_x/\text{Cu-N@CF}$ . Blue rectangles indicate Fe nanoclusters.

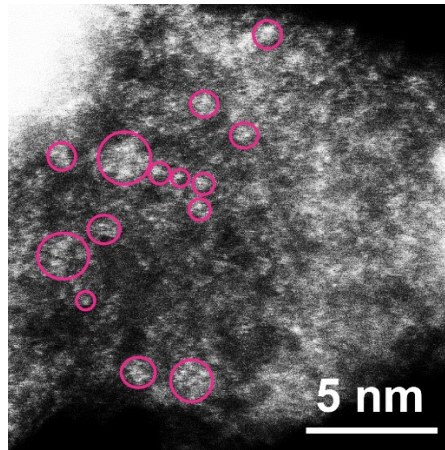


Figure S10. HAADF-STEM image of  $\text{Fe}_x\text{-N@CF}$  (marked larger spots with pink circles).



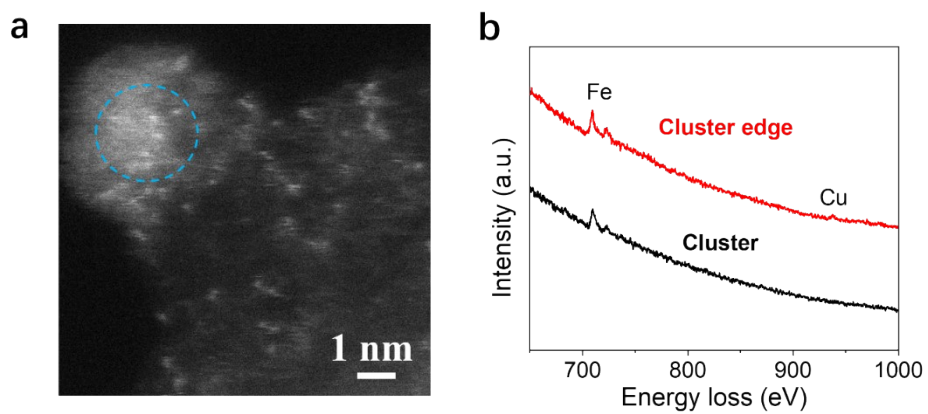


Figure S11. (a) Atomic-level HAADF-STEM image (marked the bright cluster with the blue circle), (b) corresponding EEL spectra.

Table S1. Fe and Cu content determined by ICP-OES.

Samples	Fe content (wt. %)	Cu content (wt. %)
Fe <sub>x</sub> /Cu-N@CF	2.23%	0.57%
Fe <sub>x</sub> -N@CF	2.01%	0.06%
Cu-N@CF	0.05%	0.62%

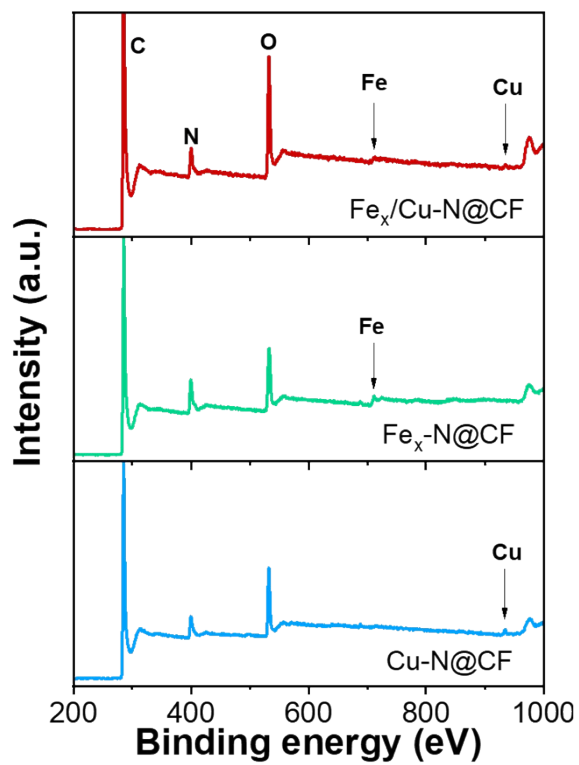


Figure S12. The wide-scanning XPS spectra of  $\text{Cu-N@CF}$ ,  $\text{Fe}_x\text{-N@CF}$  and  $\text{Fe}_x/\text{Cu-N@CF}$ .

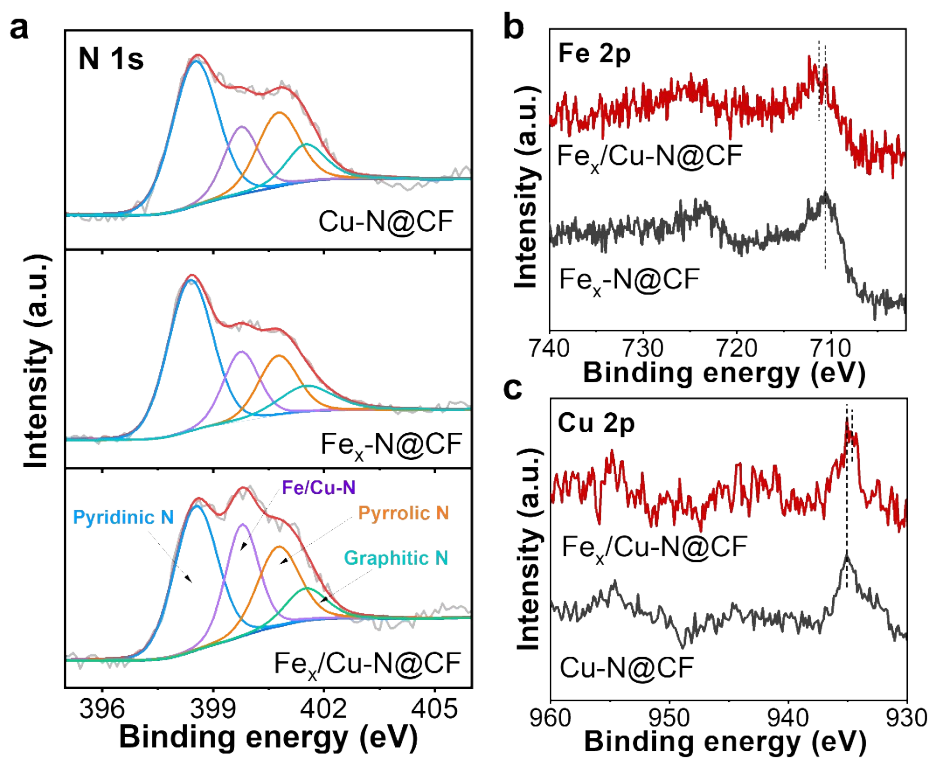


Figure S13. XPS spectra of N 1s, Fe 2p, and Cu 2p in Cu-N@CF, Fe<sub>x</sub>-N@CF and Fe<sub>x</sub>/Cu-N@CF.

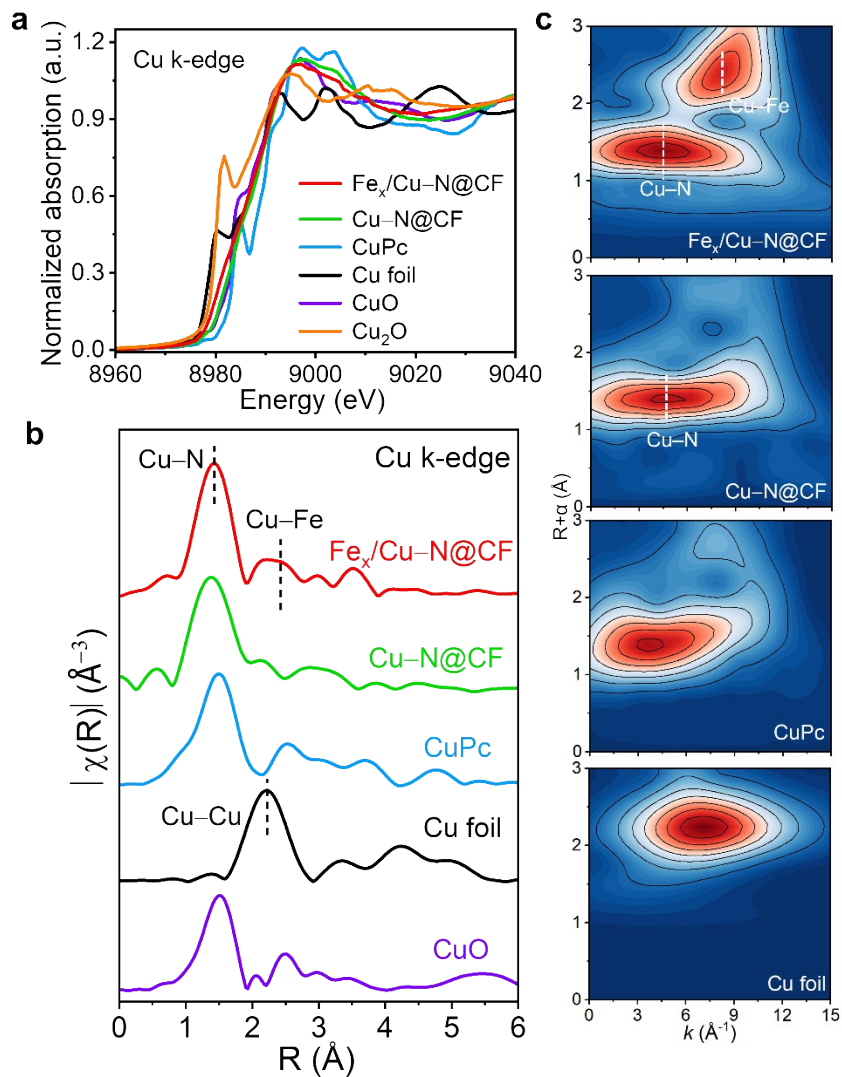


Figure S14. (a) Cu K-edge XANES spectra and (b) EXAFS curves of Fe<sub>x</sub>/Cu-N@CF, Cu-N@CF and references (Cu Pc, Cu foil, CuO, Cu<sub>2</sub>O). (c) WT-EXAFS of Fe<sub>x</sub>/Cu-N@CF, Cu-N@CF, Cu Pc, Cu foil and CuO.

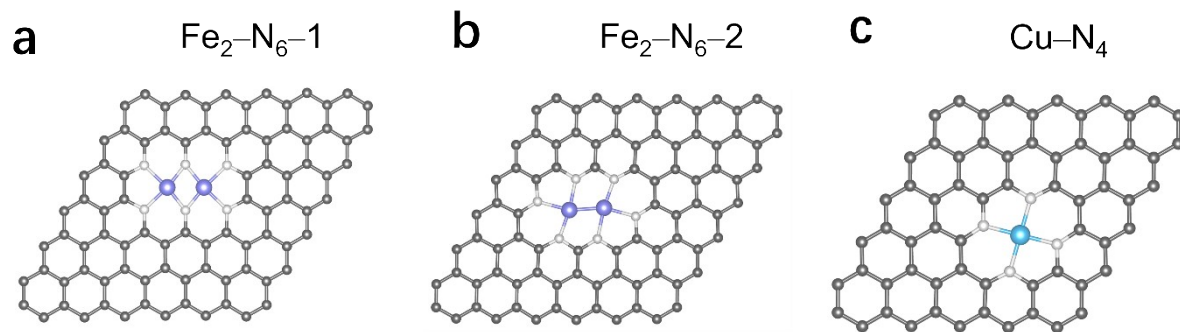


Figure S15. The proposed possible structural models of  $\text{Fe}_x\text{-N@CF}$  (a-b) and  $\text{Cu-N@CF}$  (c).

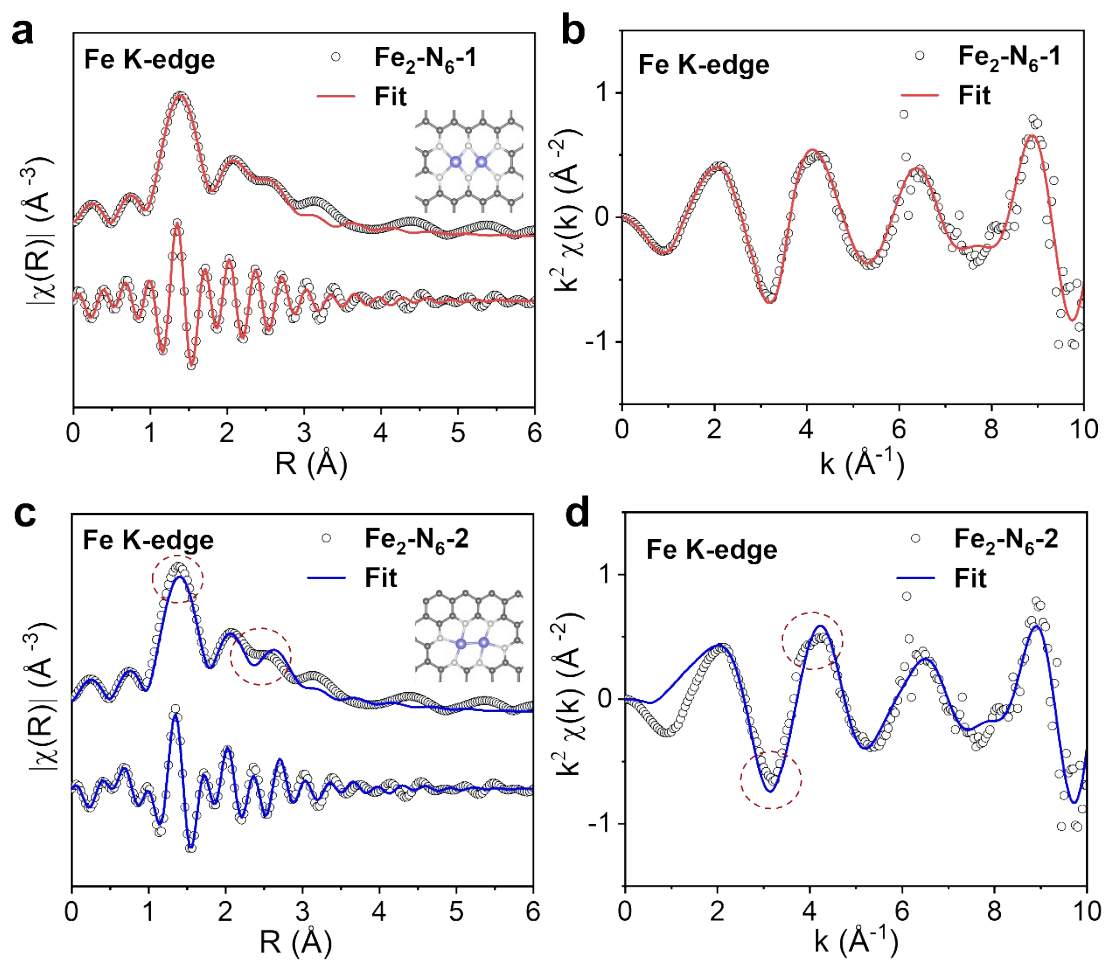


Figure S16. (a, b) Fe K-edge experimental and FT-EXAFS fitting curves of  $\text{Fe}_x\text{-N@CF}$  and the corresponding fitting curves of  $k^2$ -weighted  $k$ -space based on  $\text{Fe}_2\text{-N}_6\text{-1}$  and (c, d)  $\text{Fe}_2\text{-N}_6\text{-2}$  models.

Table S2. The Fe K-edge EXAFS curves fitting parameters of Fe<sub>x</sub>-N@CF based on Fe<sub>2</sub>-N<sub>6</sub>-1, Fe<sub>2</sub>-N<sub>6</sub>-2 models.

Sample	Scattering pair	Coordination number	R(Å)	$\sigma^2$	$\Delta E_0$	$S_0^2$	R factor
Fe <sub>2</sub> -N <sub>6</sub> -1	Fe-N1	1.98 ± 0.126	1.72	0.005	3.9	0.83	0.0032
	Fe-N2	1.89 ± 0.367	1.94	0.004			
	Fe-Fe	0.91 ± 0.161	2.18	0.003			
Fe <sub>2</sub> -N <sub>6</sub> -2	Fe-N	2.81 ± 0.69	1.99	0.003	4.5	0.83	0.029
	Fe-Fe	0.94 ± 0.39	2.22	0.003			



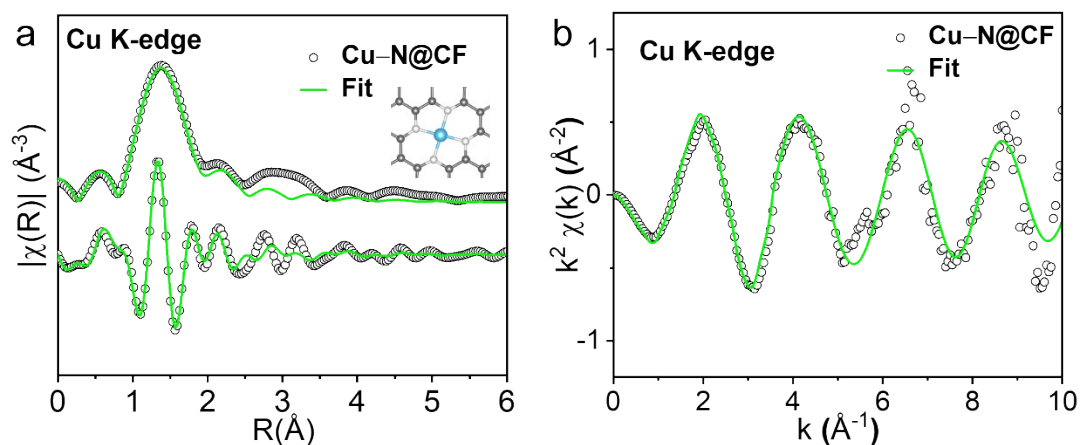


Figure S17. (a) Cu K-edge experimental and FT-EXAFS fitting curves of Cu-N@CF based on Cu-N<sub>4</sub> model. (b) The corresponding fitting curves are shown in k<sup>2</sup>-weighted k-space.

Table S3. The Cu K-edge EXAFS curves fitting parameters of Cu-N@CF.

Sample	Scattering pair	Coordination number	R(Å)	$\sigma^2$	$\Delta E_0$	$S_0^2$	R factor
Cu-N@CF	Cu-N	$3.91 \pm 0.221$	1.89	0.004	3.6	0.9	0.0044

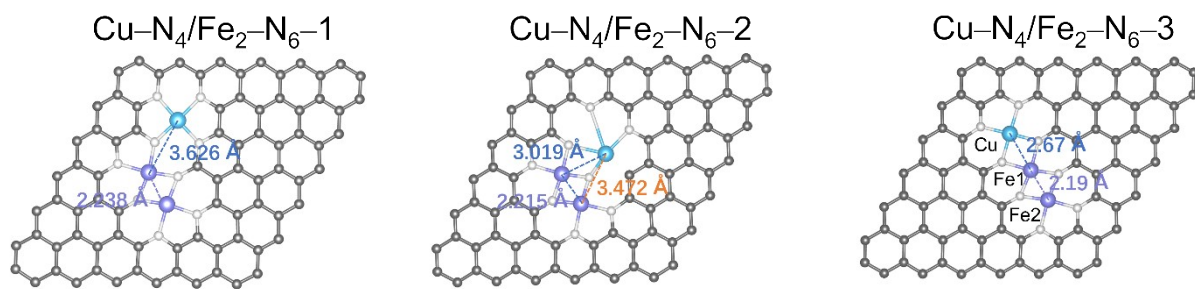


Figure S18. The possible structural models of Fe<sub>x</sub>/Cu-N@CF.

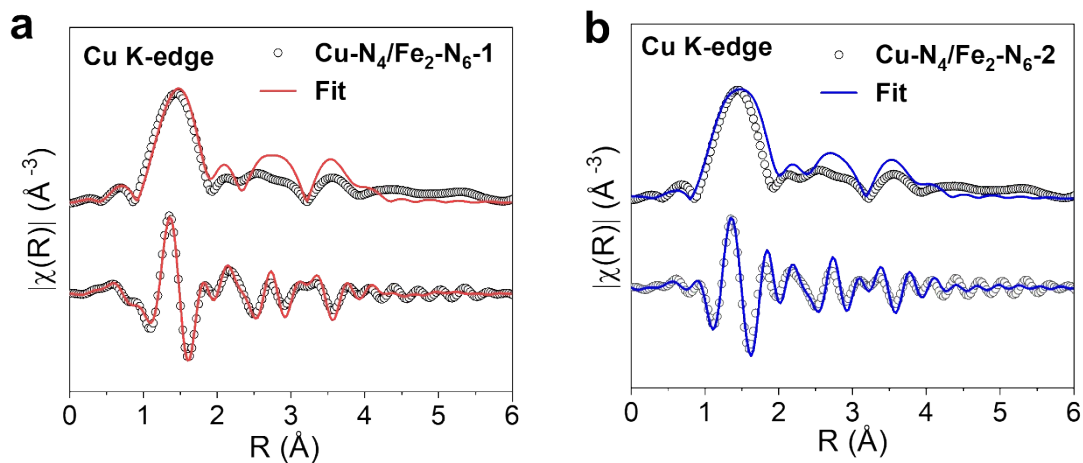


Figure S19. Cu K-edge experimental and FT-EXAFS fitting curves of Cu-N@CF based on Cu-N<sub>4</sub>/Fe<sub>2</sub>-N<sub>6</sub>-1 model (a) and Cu-N<sub>4</sub>/Fe<sub>2</sub>-N<sub>6</sub>-2 model (b).

Table S4. The Cu K-edge EXAFS curves fitting parameters of Cu-N@CF based on Cu-N<sub>4</sub>/Fe<sub>2</sub>-N<sub>6</sub>-1 and Cu-N<sub>4</sub>/Fe<sub>2</sub>-N<sub>6</sub>-2 models.

Sample	Scattering pair	Coordination number	R(Å)	$\sigma^2$	$\Delta E_0$	$S_0^2$	R factor
Cu-N <sub>4</sub> /Fe <sub>2</sub> -N <sub>6</sub> -1	Cu-N1	3.13 ± 0.132	1.95	0.003	4.2	0.9	0.043
	Cu-N2	1.02 ± 0.571	1.80	0.004			
	Cu-Fe	0.55 ± 0.461	3.23	0.006			
Cu-N <sub>4</sub> /Fe <sub>2</sub> -N <sub>6</sub> -2	Cu-N1	2.11 ± 0.159	1.97	0.004	5.5	0.9	0.031
	Cu-N2	1.74 ± 0.436	1.80	0.004			
	Cu-Fe	0.67 ± 0.387	2.89	0.006			

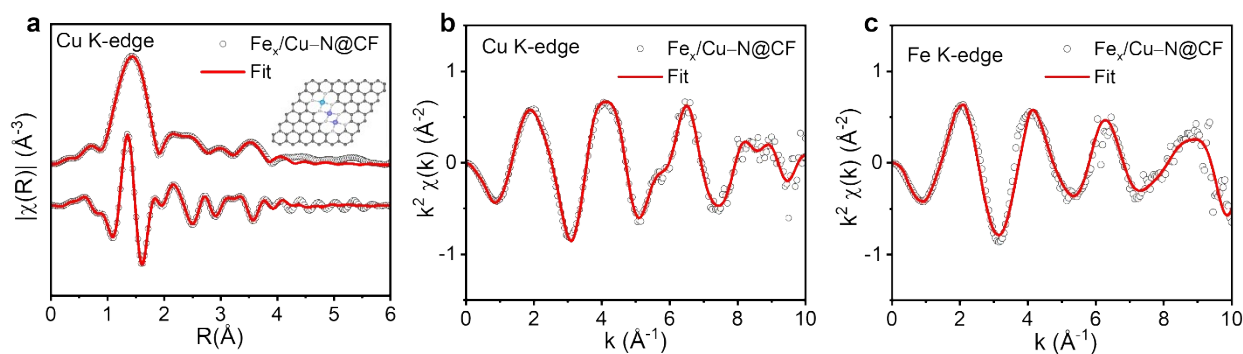


Figure S20. (a) Cu K-edge experimental and FT-EXAFS fitting curves of  $\text{Fe}_x/\text{Cu-N@CF}$  in R-space (inset shows the corresponding structure model), and (b) the corresponding fitting curve shown in  $k^2$ -weighted k-space. (c) Fe K-edge experimental and FT-EXAFS fitting curves of  $\text{Fe}_x/\text{Cu-N@CF}$  shown in  $k^2$ -weighted k-space.

Table S5. The Cu K-edge EXAFS curves fitting parameters of  $\text{Fe}_x/\text{Cu-N@CF}$ .

Sample	Scattering pair	Coordination number	R(Å)	$\sigma^2$	$\Delta E_0$	$S_0^2$	R factor
$\text{Fe}_x/\text{Cu-N@CF}$	Cu-N1	$2.99 \pm 0.041$	1.95	0.005	3.6	0.9	0.001
	Cu-N2	$0.98 \pm 0.083$	1.80	0.004			
	Cu-Fe	$1.05 \pm 0.062$	2.77	0.003			

Table S6. The Fe K-edge EXAFS curves fitting parameters of  $\text{Fe}_x/\text{Cu-N@CF}$ .

Sample	Scattering pair	Coordination number	R(Å)	$\sigma^2$	$\Delta E_0$	$S_0^2$	R factor
$\text{Fe}_x/\text{Cu-N@CF}$	Fe-N1	$2.22 \pm 0.361$	1.77	0.005	3.9	0.83	0.012
	Fe-N2	$1.85 \pm 0.123$	1.95	0.004			
	Fe-Fe	$1.13 \pm 0.345$	2.17	0.003			
	Fe-Cu	$1.15 \pm 0.514$	2.77	0.003			

R is the distance between absorber and backscatter atoms,  $\sigma^2$  is Debye-Waller factor to account for both thermal and structural disorders,  $\Delta E_0$  is inner potential correction; R factor indicates the goodness of the fit.  $S_0^2$  for Fe K-edge fitting was fixed to 0.83 determined from

Fe foil fitting.  $S_0^2$  for Cu K-edge fitting was fixed to 0.9 determined from Cu foil. Fitting range:  $3 \leq k (\text{\AA}^{-1}) \leq 11$  and  $1 \leq R (\text{\AA}) \leq 3$ .

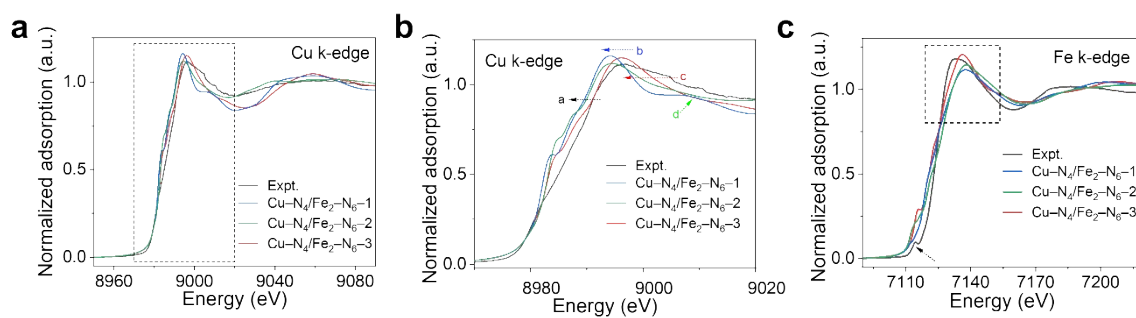


Figure S21. (a) Comparison between the experimental Cu K-edge XANES spectrum of  $\text{Fe}_x/\text{Cu-N@CF}$  and the simulated spectra. (b) The spectra from dash box of (a). (c) Comparison between the experimental Fe K-edge XANES spectrum of  $\text{Fe}_x/\text{Cu-N@CF}$  and the simulated spectra.

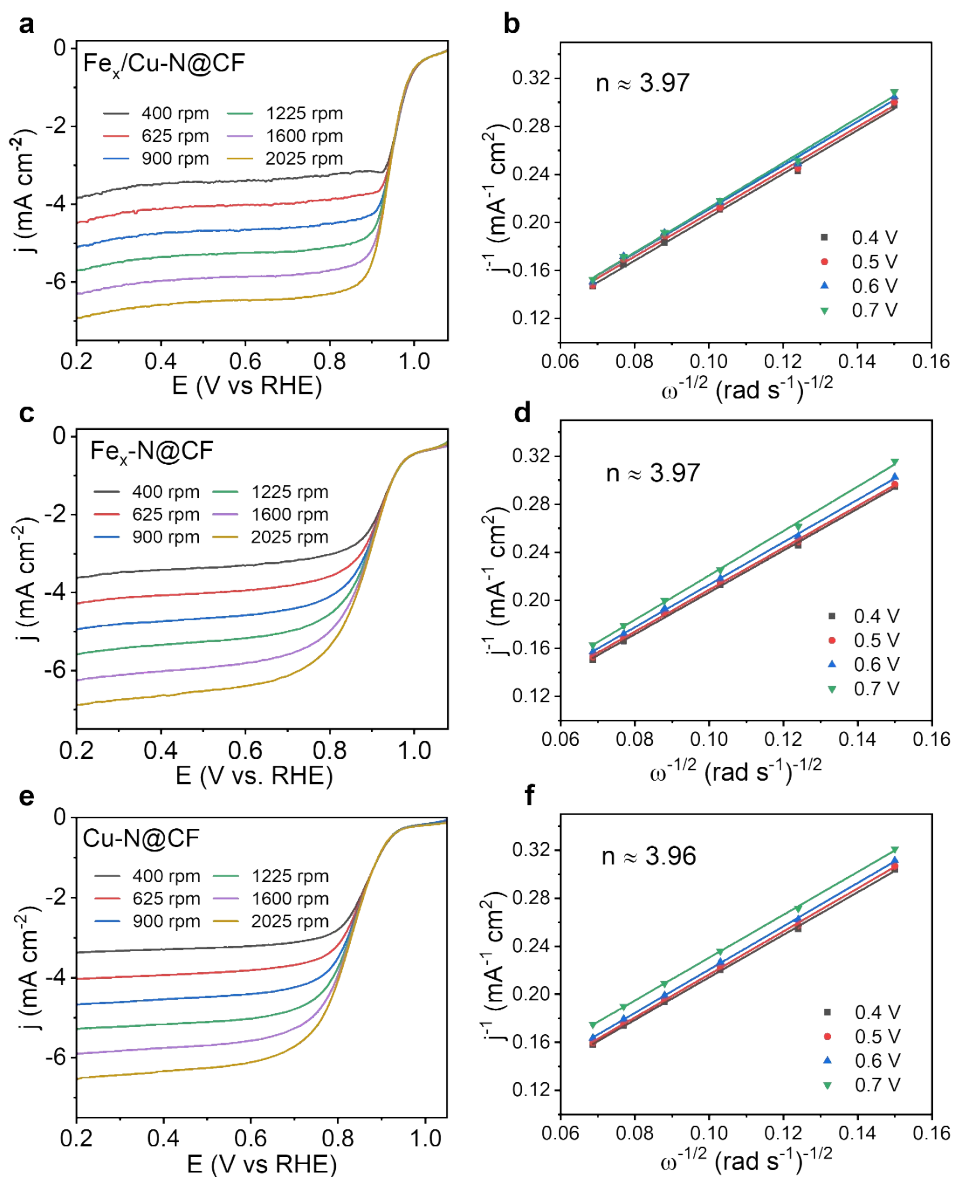


Figure S22. LSV curves of (a) Fe<sub>x</sub>/Cu-N@CF, (c) Fe<sub>x</sub>-N@CF and (e) Cu-N@CF at different rotating rates. (b, d, f) The corresponding K-L plots and electron transfer number.

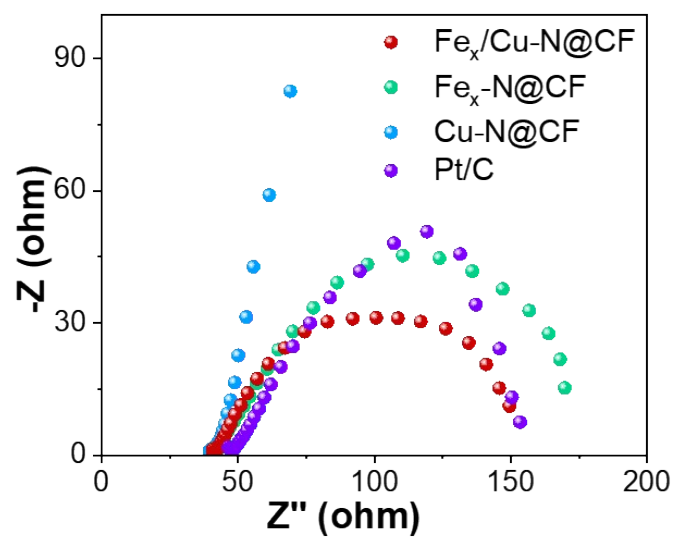


Figure S23. EIS plots of Fe<sub>x</sub>/Cu-N@CF, Fe<sub>x</sub>-N@CF, Cu-N@CF and Pt/C.



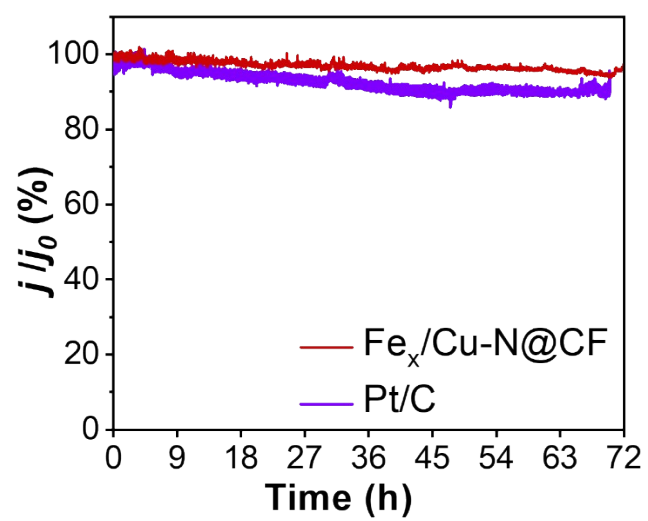


Figure S24. Stability test at 0.6 V for  $\text{Fe}_x/\text{Cu-N@CF}$  and Pt/C in 0.1 M KOH.

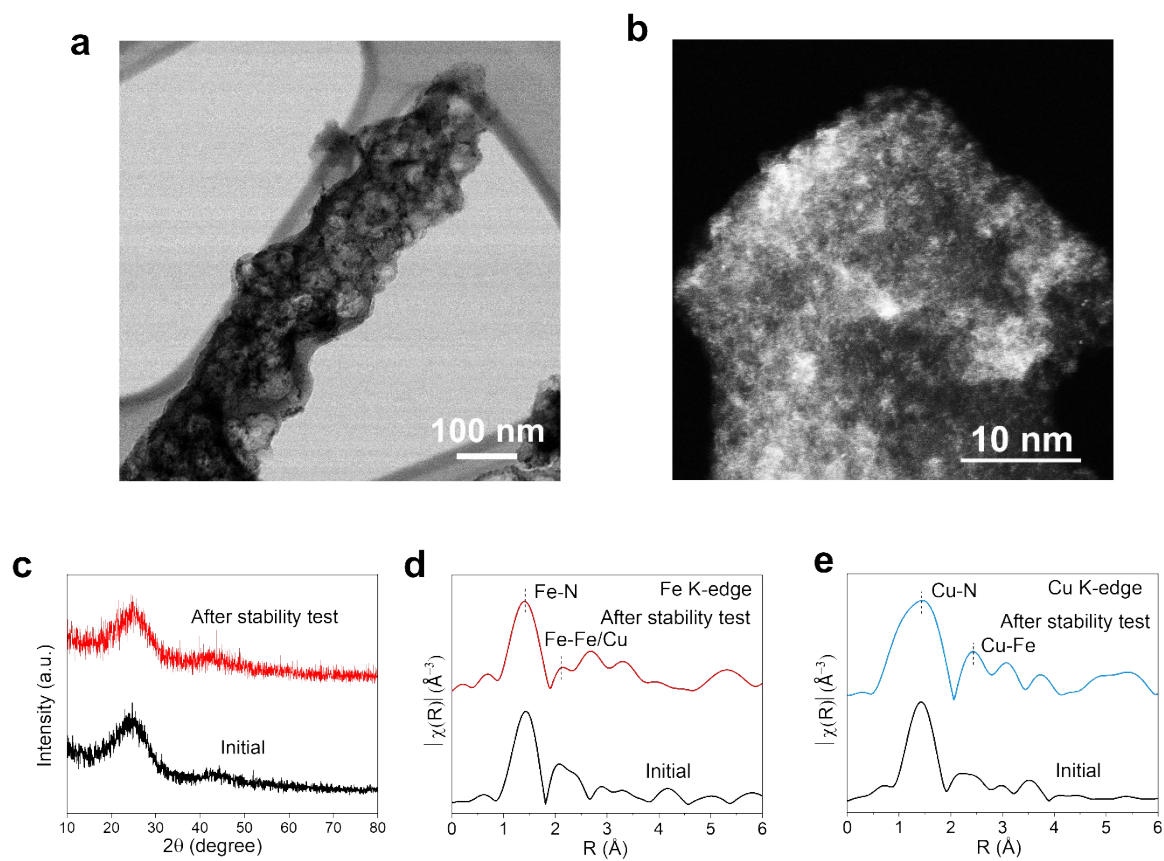


Figure S25. (a-b) HR-TEM image, (c) XRD pattern, (d-e) Fourier-transform EXAFS curves of  $\text{Fe}_x/\text{Cu-N@CF}$  before and after stability test.

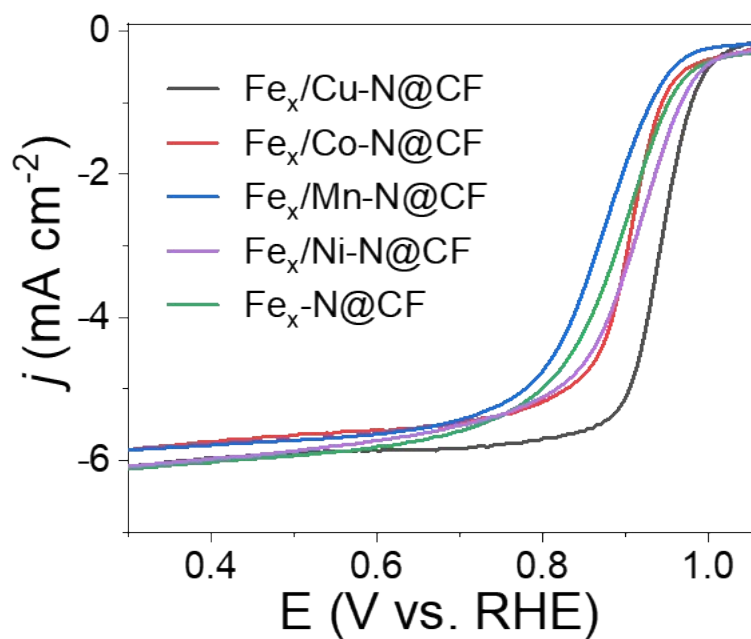


Figure 26. LSV curves were recorded in 0.1 M KOH with a rotation rate of 1600 rpm.

The ORR performance of other  $\text{M-N}_4$  (e.g.,  $\text{CoN}_4$ ,  $\text{MnN}_4$ , and  $\text{NiN}_4$ ) decorated atomic Fe clusters was also examined. As shown in Figure S26, the  $\text{CuN}_4$  is the most effective one in improving the ORR performance of Fe clusters.

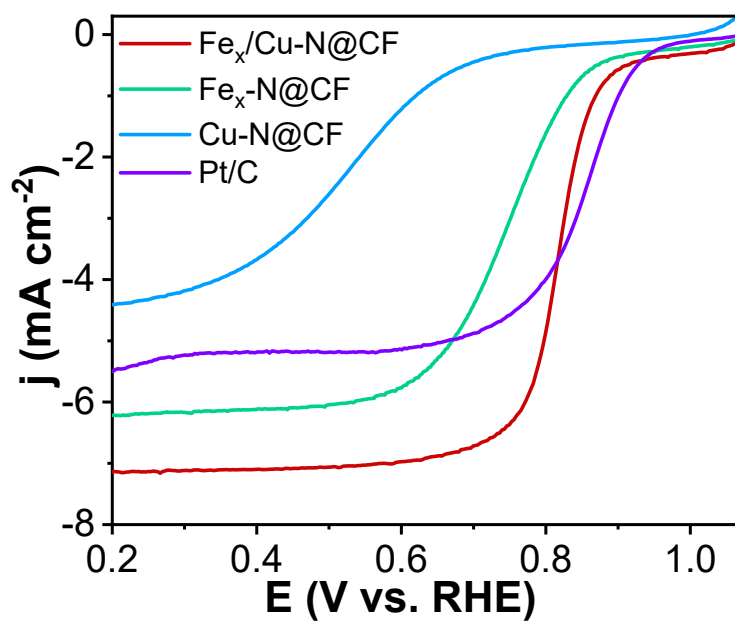


Figure S27. LSV curves in O<sub>2</sub>-saturated 0.1 M HClO<sub>4</sub>.

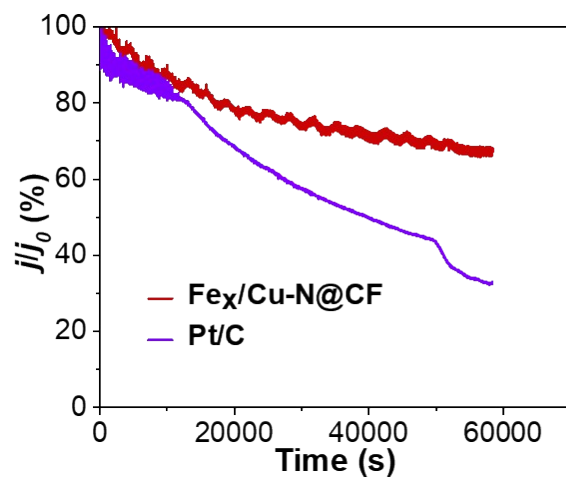


Figure S28. Stability test at 0.6 V in 0.1 M HClO<sub>4</sub>.

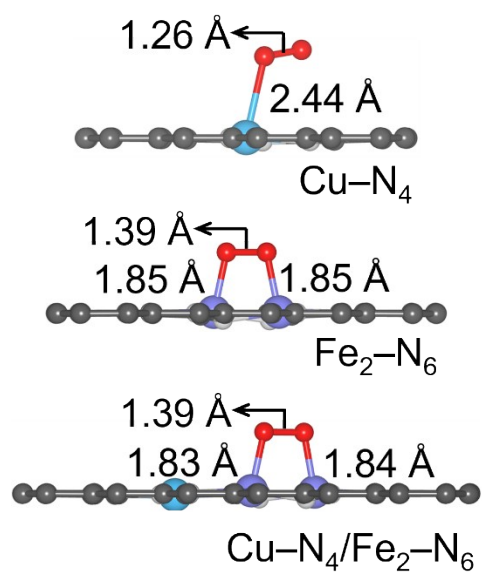


Figure S29. Optimized geometry of OO\* adsorption configuration on Cu-N<sub>4</sub>, Fe<sub>2</sub>-N<sub>6</sub> and Cu-N<sub>4</sub>/Fe<sub>2</sub>-N<sub>6</sub>.

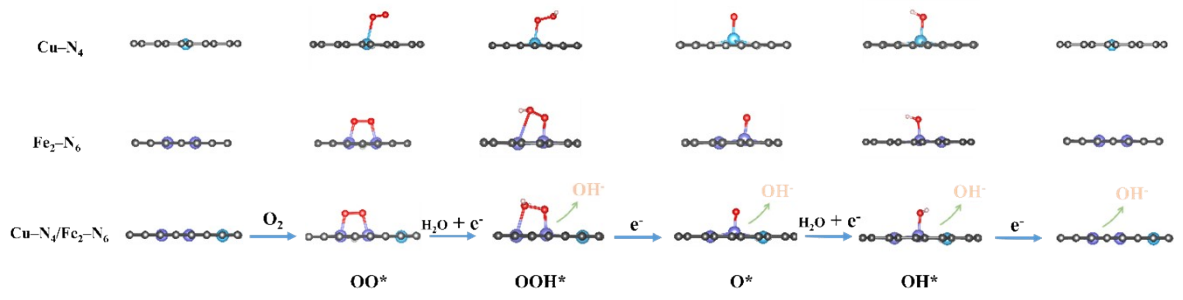


Figure S30. The ORR reaction pathways of Cu-N<sub>4</sub>, Fe<sub>2</sub>-N<sub>6</sub> and Cu-N<sub>4</sub>/Fe<sub>2</sub>-N<sub>6</sub>.

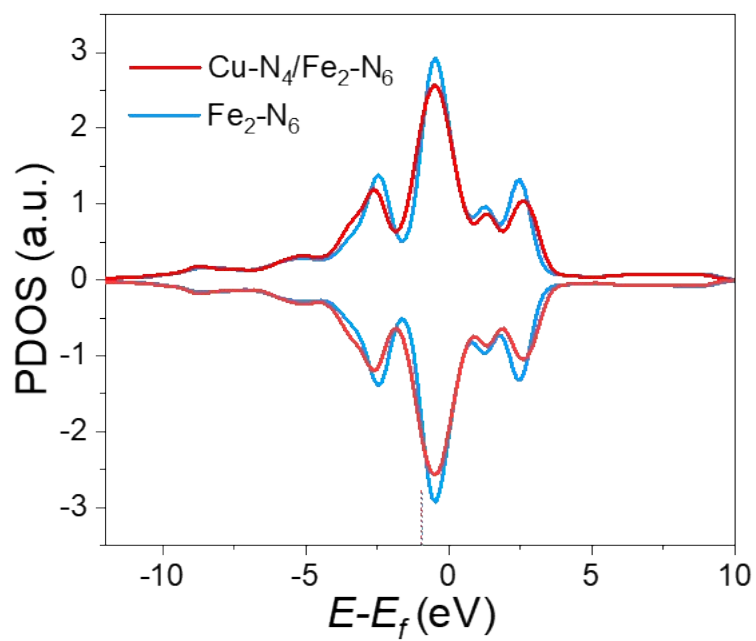
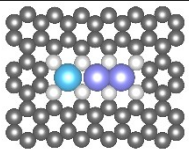
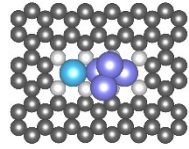
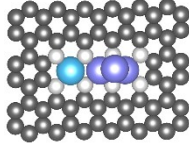
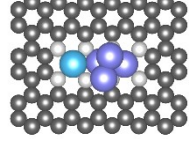


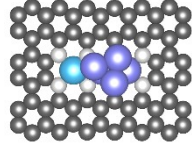
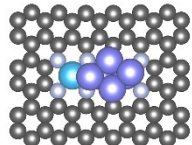
Figure S31. The PDOS of Fe *d* orbitals in Fe<sub>2</sub>-N<sub>6</sub> and Cu-N<sub>4</sub>/Fe<sub>2</sub>-N<sub>6</sub>.



Additional DFT calculations were performed to investigate the possible structure of the catalyst. To investigate the thermodynamic feasibility of Fe forming a cluster with a larger number of atoms, we calculated the reaction energy of adding Fe to the CNF structure, starting from Cu-N<sub>4</sub>/N<sub>6</sub> and progressing to Cu-N<sub>4</sub>/Fe<sub>2</sub>-N<sub>6</sub>, and all the way to Cu-N<sub>4</sub>/Fe<sub>6</sub>-N<sub>6</sub>. Table S7 reports the reaction energies. The comparison of reactions i and ii reveals that the addition of first two Fe atoms close to Cu is energetically favorable (-3.50 eV). However, if Cu-N<sub>4</sub>/Fe<sub>2</sub>-N<sub>6</sub> is already formed, adding two more Fe atoms is significantly less favorable, suggesting it is unlikely to occur on the catalytic surface. As Fe atoms are added one by one to the previous structures in reactions iii-vi, the reaction energies increase from +2.53 to +2.93 eV, indicating that during the catalyst synthesis, Fe atoms are more likely to form a new Cu-N<sub>4</sub>/Fe<sub>2</sub>-N<sub>6</sub> structure near a single Cu with the formation of Fe-N moieties on the CNF rather than aggregating into larger Fe-Fe clusters.

Table S7. The Fe cluster formation reactions and corresponding reaction energies

	Hypothetical reactions	Reaction energy(eV)	Structures
i	$\text{Cu-N}_4/\text{N}_6 + 2\text{Fe} = \text{Cu-N}_4/\text{Fe}_2\text{-N}_6$	-3.50	
ii	$\text{Cu-N}_4/\text{Fe}_2\text{-N}_6 + 2\text{Fe} = \text{Cu-N}_4/\text{Fe}_4\text{-N}_6$	+5.27	
iii	$\text{Cu-N}_4/\text{Fe}_2\text{-N}_6 + \text{Fe} = \text{Cu-N}_4/\text{Fe}_3\text{-N}_6$	+2.53	
iv	$\text{Cu-N}_4/\text{Fe}_3\text{-N}_6 + \text{Fe} = \text{Cu-N}_4/\text{Fe}_4\text{-N}_6$	+2.73	

v	$\begin{array}{l} \text{Cu-N}_4/\text{Fe}_4\text{-N}_6 \\ \text{Cu-N}_4/\text{Fe}_5\text{-N}_6 \end{array} + \text{Fe} =$	+2.70	
vi	$\begin{array}{l} \text{Cu-N}_4/\text{Fe}_5\text{-N}_6 \\ \text{Cu-N}_4/\text{Fe}_6\text{-N}_6 \end{array} + \text{Fe} =$	+2.93	

\*The energy of Fe is taken from pure iron lattice unit cell.

The use of simplified models with a few Fe atoms to represent an iron cluster is common in the literature.<sup>21,22</sup> We believe that the Cu-N<sub>4</sub>/Fe<sub>2</sub>-N<sub>6</sub> model is appropriate as a basic unit for representing the catalyst structure. To validate this model, we calculated the free energy pathway of a larger model consisting of Cu-N<sub>4</sub>/Fe<sub>4</sub>-N<sub>11</sub> (Figure S32). The Cu-N<sub>4</sub>/Fe<sub>4</sub>-N<sub>11</sub> model has single Cu atoms located on the edges of the observed "Fe cluster."

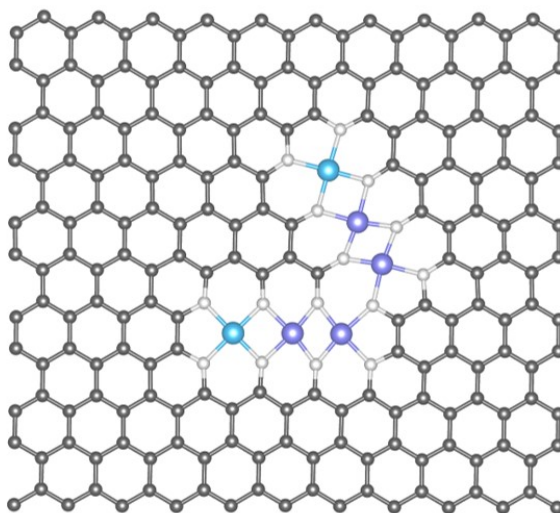


Figure S32. The Cu-N<sub>4</sub>/Fe<sub>4</sub>-N<sub>11</sub> model.

We found that the active site remains on the Fe atoms that are closest to the Cu atoms, confirming the enhancing effect of Cu on the reactivity of the Fe cluster. As shown in Figure S33, the energy profile of this large model is similar to the Cu-N<sub>4</sub>/Fe<sub>2</sub>-N<sub>6</sub> model proposed in the manuscript, with a similar limiting step of 0.62 eV (the reaction energy for \*OO to \*OOH). This suggests that the combination of multiple Cu-N<sub>4</sub>/Fe<sub>2</sub>-N<sub>6</sub> models could potentially form a large Fe cluster in the center with single Cu atoms on the edges, while still maintaining active sites on Fe atoms that are enhanced by Cu atoms. Therefore, we conclude that the Cu-N<sub>4</sub>/Fe<sub>2</sub>-N<sub>6</sub> model proposed is suitable for representing the catalyst structure.

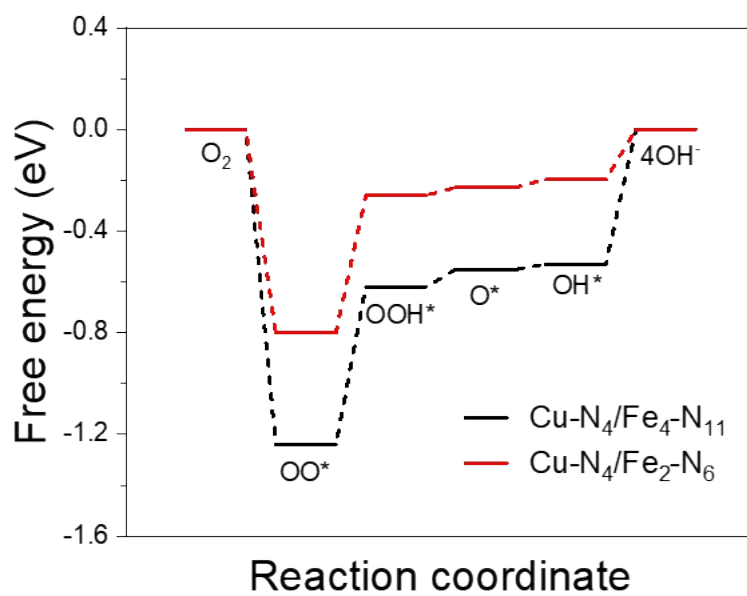


Figure S33. ORR free energy diagrams for Cu-N<sub>4</sub>/Fe<sub>2</sub>-N<sub>6</sub>, and Cu-N<sub>4</sub>/Fe<sub>4</sub>-N<sub>11</sub> at U=1.23 V.

Table S8. Bader's charge of Fe atom on Fe<sub>2</sub>-N<sub>6</sub> and Cu-N<sub>4</sub>/Fe<sub>2</sub>-N<sub>6</sub> model

Model	Fe #1	Fe #2	Average
Fe <sub>2</sub> -N <sub>6</sub>	0.959	0.956	0.958
Cu-N <sub>4</sub> /Fe <sub>2</sub> -N <sub>6</sub>	1.015	0.984	1.000

Bader's charge analysis was performed to further investigate the impact of Cu on Fe<sub>2</sub>-N<sub>6</sub>. Table S8 shows the Bader's charge for Fe on both Fe<sub>2</sub>-N<sub>6</sub> and Cu-N<sub>4</sub>/Fe<sub>2</sub>-N<sub>6</sub> models. On Fe<sub>2</sub>-N<sub>6</sub> model, two Fe atoms have the same neighbor atoms, resulting in their Bader's charges being similar, with an average value of 0.958. On Cu-N<sub>4</sub>/Fe<sub>2</sub>-N<sub>6</sub> model, the Bader's charges of Fe are slightly increased to 1.015 and 0.984, respectively. We observed Fe #1 is in between Cu and another Fe atom (Fe #2). As Fe #1 is closer to Cu, its Bader's charge increased more significantly, resulting in a stronger bond with O-containing adsorbates. This is qualitatively in agreement with configuration analysis and free energy calculation results.

Table S9. ORR activities of various transition metal single-atom electrocatalysts in 0.1 M KOH.

Catalysts	$E_{1/2}$ (V vs RHE)	Tafel slope (mV dec <sup>-1</sup> )	$J_k$ (mA cm <sup>-2</sup> ) @0.9 (V vs RHE)*	MA(A g <sup>-1</sup> )@ @0.9 (V vs RHE)*	Reference
<b>Fe<sub>x</sub>/Cu-N@CF</b>	<b>0.944</b>	<b>52.61</b>	<b>34.37</b>	<b>137.5</b>	<b>This work</b>
NCAG/Fe-Cu	0.94	55	20	49.1	23
Fe/Zn-N-C	0.906	47	10	26.3	24
Fe-Te <sub>n</sub>	0.867	86	2.3	20.3	25
Co <sub>2</sub> /Fe-N@CHC	0.915	62	9.44	31.46	26
Fe <sub>3</sub> Mn/N-C	0.928	86	7.1	71	27
Cu/Zn-NC	0.83	54.8	1.1	2.71	28
Zn/Fe-N-C	0.86	84	5.49@0.85V	16.1@0.85V	29
Fe-N <sub>4</sub> /Pt-N <sub>4</sub> @NC	0.93	78	13.1	NA	30
Ni-N <sub>4</sub> /GHSs/Fe-N <sub>4</sub>	0.83	55	2.8	11.2	31
Fe/Ni-N <sub>x</sub> /OC	0.938	59.9	28.1	98.6	32
FeCoNiCuMn	0.887	81	3.2	6.27	33
Fe-NC-S	0.88	49	2	10	34
Fe-N/P-C-700	0.844	NA	1.56	2.6	35
Fe/SNCFs-NH <sub>3</sub>	0.89	70.82	38.36 @ 0.82 V	100.2@0.82	36
Fe-Pc-O defect	0.929	30	13	118.4	37
Fe-N-C-900	0.905	76.6	10	50	38
Fe-N-C/Fe NP	0.885	56	55.1 @ 0.8 V	162.1@0.8V	39
FeAC@FeSA-N-C	0.912	61	61.1@0.85	165@0.85	40
Fe-ACSA@NC	0.90	76	6.45	24.81	41
P/Fe-N-C	0.90	NA	25.4@0.85	40.7@0.85	42
5-PtNi <sub>x</sub> /NiNC	0.86	NA	NA	26	43
Pd <sub>50</sub> Ag <sub>50</sub>	0.81	45.7	NA	NA	44

\*The value of  $J_k$  and Mass activity (MA) are recorded at 0.9 V, except specifically noted.

## References

1. D. C. Koningsberger and R. Prins, 1987.
2. B. Ravel and M. Newville, *J. Synchrotron Radiat*, 2005, **12**, 537-541.
3. H. Funke, A. Scheinost and M. Chukalina, *Phys. Rev. B*, 2005, **71**, 094110.
4. H. Funke, M. Chukalina and A. Scheinost, *J. Synchrotron Radiat*, 2007, **14**, 426-432.
5. O. Bunău, A. Y. Ramos and Y. Joly, *Wiley*, 2021.
6. Y. Joly, A. Y. Ramos and O. Bunău, *Wiley*, 2022.
7. S. Niu, S. Li, Y. Du, X. Han and P. Xu, *ACS Energy Lett*, 2020, **5**, 1083-1087.
8. S. G. Ji, H. Kim, C. Park, W. Kim and C. Choi, *ACS Catal.*, 2020, **10**, 10773-10783.
9. G. Yang, J. Zhu, P. Yuan, Y. Hu, G. Qu, B.-A. Lu, X. Xue, H. Yin, W. Cheng, J. Cheng and W. Xu, *Nat. Commun.*, 2021, **12**, 1734.
10. G. Kresse and J. Furthmüller, *Comput. Mater. Sci.*, 1996, **6**, 15-50.
11. G. Kresse and J. Furthmüller, *Phys. Rev. B*, 1996, **54**, 11169-11186.
12. G. Kresse and J. Hafner, *J. Phys. Condens. Matter*, 1994, **6**, 8245-8257.
13. G. Kresse and D. Joubert, *Phys. Rev. B*, 1999, **59**, 1758-1775.
14. G. Kresse and J. Hafner, *Phys. Rev. B*, 1993, **47**, 558-561.
15. P. E. Blöchl, *Phys. Rev. B*, 1994, **50**, 17953-17979.
16. J. P. Perdew, K. Burke and M. Ernzerhof, *Phys. Rev. Lett.*, 1996, **77**, 3865-3868.
17. J. Klimeš, A. Bowler Dr Fau - Michaelides and A. Michaelides, *Condens. Matter*, 2009, **22**, 022201.
18. J. Klimeš, D. R. Bowler and A. Michaelides, *Phys. Rev. B*, 2011, **83**, 195131.
19. Malcolm W. Chase, Jr., *NIST-JANAF thermochemical tables*, Fourth edition. Washington, DC : American Chemical Society ; New York : American Institute of Physics for the National Institute of Standards and Technology, 1998.
20. J. K. Nørskov, J. Rossmeisl, A. Logadottir, L. Lindqvist, J. R. Kitchin, T. Bligaard and H. Jónsson, *J. Phys. Chem. B*, 2004, **108**, 17886-17892.
21. X. Wan, Q. Liu, J. Liu, S. Liu, X. Liu, L. Zheng, J. Shang, R. Yu and J. Shui, *Nat. commun.*, 2022, **13**, 2963.
22. S. An, G. Zhang, T. Wang, W. Zhang, K. Li, C. Song, J. T. Miller, S. Miao, J. Wang and X. Guo, *ACS nano*, 2018, **12**, 9441-9450.

23. T. He, Y. Chen, Q. Liu, B. Lu, X. Song, H. Liu, M. Liu, Y. N. Liu, Y. Zhang and X. Ouyang, *Angew. Chem. Int. Ed.*, 2022, **61**, e202201007.
24. H. Li, S. Di, P. Niu, S. Wang, J. Wang, L. Li, *Energy Environ. Sci.*, 2022, **15**, 1601-1610.
25. B. Ji, J. Gou, Y. Zheng, X. Zhou, P. Kidkhunthod, Y. Wang, Q. Tang and Y. Tang, *Adv. Mater.*, 2022, **34**, 2202714.
26. Z. Wang, X. Jin, C. Zhu, Y. Liu, H. Tan, R. Ku, Y. Zhang, L. Zhou, Z. Liu, S. J. Hwang and H.J. Fan, *Adv. Mater.*, 2021, **33**, 2104718.
27. G. Yang, J. Zhu, P. Yuan, Y. Hu, G. Qu, B.-A. Lu, X. Xue, H. Yin, W. Cheng, J. Cheng and W. Xu, *Nat. Commun.*, 2021, **12**, 1-10.
28. M. Tong, F. Sun, Y. Xie, Y. Wang, Y. Yang, C. Tian, L. Wang and H. Fu, *Angew. Chem. Int. Ed.*, 2021, **60**, 14005-14012.
29. J. Xue, Y. Li and J. Hu, *J. Mater. Chem. A*, 2020, **8**, 7145-7157.
30. A. Han, X. Wang, K. Tang, Z. Zhang, C. Ye, K. Kong, H. Hu, L. Zheng, P. Jiang, C. Zhao and Q. Zhang *Angew. Chem. Int. Ed.*, 2021, **60**, 19262-19271.
31. J. Chen, H. Li, C. Fan, Q. Meng, Y. Tang, X. Qiu, G. Fu and T. J. A. M. Ma, *Adv. Mater.*, 2020, **32**, 2003134.
32. Z. Zhu, H. Yin, Y. Wang, C. H. Chuang, L. Xing, M. Dong, Y. R. Lu, G. Casillas-Garcia, Y. Zheng, S. Chen and Y. Dou, *Adv. Mater.*, 2020, **32**, 2004670.
33. Rao, P., Deng, Y., Fan, W. *et al.* Movable type printing method to synthesize high-entropy single-atom catalysts. *Nat Commun.*, 2022, **13**, 5071.
34. X. Li, C.-S. Cao, S.-F. Hung, Y.-R. Lu, W. Cai, A. I. Rykov, S. Miao, S. Xi, H. Yang and Z. J. C. Hu, 2020, **6**, 3440-3454.
35. K. Yuan, D. Lützenkirchen-Hecht, L. Li, L. Shuai, Y. Li, R. Cao, M. Qiu, X. Zhuang, M. K. Leung and Y. J. J. o. t. A. C. S. Chen, 2020, **142**, 2404-2412.
36. L. Yang, X. Zhang, L. Yu, J. Hou, Z. Zhou and R. Lv, *Adv. Mater.*, 2022, **34**, 2105410.
37. X. Tan, H. Li, W. Zhang, K. Jiang, S. Zhai, W. Zhang, N. Chen, H. Li and Z. Li, *Chem Catal.*, 2022, **2**, 816-835.
38. C. Zhu, Q. Shi, B. Z. Xu, S. Fu, G. Wan, C. Yang, S. Yao, J. Song, H. Zhou, D. Du and S.P. Beckman, *Adv. Energy Mater.*, 2018, **8**, 1801956.
39. S. N. Zhao, J. K. Li, R. Wang, J. Cai and S. Q. Zang, *Adv. Mater.*, 2022, **34**, 2107291.
40. X. Ao, W. Zhang, Z. Li, J.-G. Li, L. Soule, X. Huang, W.-H. Chiang, H. M. Chen, C. Wang, M. Liu and X.C. Zeng, *ACS nano*, 2019, **13**, 11853-11862.

41. H. Huang, D. Yu, F. Hu, S. C. Huang, J. Song, H. Y. Chen, L. L. Li and S. J. A. C. Peng, *Angew. Chem. Int. Ed.*, 2022, **134**, e202116068.
42. Y. Zhou, R. Lu, X. Tao, Z. Qiu, G. Chen, J. Yang, Y. Zhao, X. Feng, K. J. J. o. t. A. C. S. Müllen, *J. Am. Chem. Soc.*, 2023, **145**, 3647-3655.
43. Q. Feng, X. Wang, M. Klingenhof, M. Heggen and P. Strasser, *Angew. Chem. Int. Ed.*, 2022, 61, e202203728.
44. W. He, X. Li, Z. Qian, Z. Liu and Z. Tang, *Int. J. Electrochem. Sci*, 2019, 14, 8781-8792.